Nanostructural synergism as Mn—N—C channels in manganese (IV) oxide and fluffy g-C$_3$N$_4$ layered composite with exceptional catalytic capabilities

Ammar Bin Yousaf [a,*], Sifani Zavahir [a], Akif Zeb [b], Alena Michalcova [c], Peter Kasak [a,*]

[a] Center for Advanced Materials, Qatar University, Doha 2713, Qatar
[b] School of Physics and Telecommunication Engineering, South China Normal University, Guangzhou, Guangdong 51006, PR China
[c] Department of Metals and Corrosion Engineering, University of Chemistry and Technology in Prague, Technicka 5, Prague 6, 166 28, Czech Republic

GRAPHICAL ABSTRACT
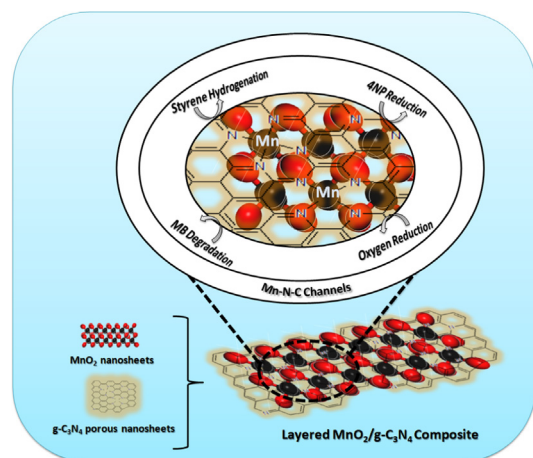
ARTICLE INFO

ABSTRACT

The avenues of catalysis and material science are always accepted and it is hoped that a state-of-the-art catalyst with exceptional intrinsic redox characteristics would be produced. This study focused on developing a multi-featured catalyst of high economical and commercial standards to meet the multi-directional applications of environmental and energy demands. Manganese (IV) oxide nanosheets made of fluffy-sheet-like g-C$_3$N$_4$ material were successfully synthesized by pyrolysis method. The electron-rich g-C$_3$N$_4$ network and semiconducting metallic oxides of MnO$_2$ nanosheets generated high electron density interfaces within the intra-composite structure. The input of active interfaces along with strong metal-to-support interactions achieved between two parallel nanosheets in MnO$_2$/g-C$_3$N$_4$ catalyst intrinsically boosted up its electrochemical and optical characteristics for it to be used in multi-catalytic fields. Successful trails of catalysts' performance have been made in three major catalytic fields with enhanced activities such as heterogeneous catalysis (reduction of nitrobenzene with rate constant of "K = 0.734 min^{-1}" and hydrogenation of styrene with "100% conversion" efficiency, including negligible change in five consecutive cycles), photocatalysis (degradation of methylene blue dye model within 20 min with negligible change in five consecutive cycles) and electrocatalysis (oxygen reduction reactions having

* Corresponding authors.
  E-mail addresses: ammar@mail.ustc.edu.cn, ammar.chemist18@gmail.com (A. Bin Yousaf), peter.kasak@qu.edu.qa (P. Kasak).

comparable "diffusion-limited-current density" behaviour with that of the commercial Pt/C catalyst). The enhanced performance of catalysts in transforming chemicals, degrading organic pollutant species and producing sustainable energy resources from air oxygen can mitigate the challenges faced in environmental and energy crises, respectively.

1. Introduction

The development of human societies has resulted in multiple environmental and energy crises for the next generation spell. There are various strategies that can be used to deal with the environmental issues either by converting pollutants into useful industrial processes or by degrading them completely into less hazardous species [1–3]. The issues related to energy sectors were addressed by introducing renewable energy resources to produce environmental friendly fuels and to stop the further consumption of fossil fuels [4,5]. Among all the strategies that have been adopted, catalysis has remained a basic tool used for each applicable scenario. Furthermore, in examining the good performances of catalysis, it has been found that catalysts play a key role in opening up facile routes. Till date, the above discussed scientific tasks have been made by various noble and non-noble metal elements and their combinations from bulk to nanoscale level [6–9].

Although there are a lot of success stories related to the development of catalysts s, there are various factors that hinder their potential utilization. These factors need to be considered for the development of this key constituent of catalysis such as, selection of materials that are cheap, environmental friendly and abundant in nature, that can be utilized at upscale projects, and have enhanced durable catalytic performance with state-of-the-art phenomenon [10–12]. In designing catalysts, carbon and carbon-based 2D graphitic material have been extensively used in the form of carbon black, carbon nanotubes and graphene to fabricate the metallic nanoparticles on their surface to boost electrons in the active sites. In this regard, graphitic materials doped with heteroatom elements (i-e nitrogen, sulphur, phosphorous) have made their debut as excellent supporting materials for metallic nanoparticles [13–16]. Among these, nitrogen doped graphitic network (g-C_3N_4) is a prestigious choice because it has similar chemistry with graphene. However, its other exceptional chemical properties (i-e electronic and optical) make it higher than 2D materials, thus t has various applications in sustainable and renewable energy and environment sectors [17,18].

The interactions of g-C_3N_4 network with metallic components in the form of composites led to the development of high electron density framework within the material by strong electron transfer system. This occurs through their connection with semiconducting metallic oxides particles [19–21]. In these interactions, the parallel faced metallic oxides nanosheets (with 2D features) and g-C_3N_4 porous sheets-like structures may constitute the interfaces within the catalyst materials [19,22]. These interfaces synergistically enhance the electrochemical and photo responsive features of catalysts, making them suitable candidates for selective applications from optoelectronics-to-organic conversion systems. Furthermore, the g-C_3N_4 materials generate strong metal-to-support interactions with metallic and non-metallic oxide materials due to their delocalized π-conjugated system that contains a number of coordination sites acting as nitrogen atoms in network; here the six-nitrogen lone-pair electrons coordinate the metal ions within the plane of highly ordered tris-triazine (C_6N_7) moieties attached through planar aromatic nitrogen-based groups [23–25].

The selection of appropriate semiconducting band structures combined with g-C_3N_4 highly improves the charge separation efficiency and redox behaviour due to the electro- or photo-induced phenomenon in catalysis. Herein, manganese oxide (MnO_2) consisting of nanosheets was used to form the nanocomposite with g-C_3N_4 fluffy sheets, which was developed as an intra-interfacial-material catalyst. MnO_2 was considered suitable due to its low-cost, high stability, compatibility with the environment and abundance in nature. In a more scientific way, MnO_2 nanostructure has strong ability to act as good adsorbent for organic molecules and volatile organic species due to its octahedral [MnO_6] structure that has large surface area and high redox potential value. In addition to its chemical composition and crystal structure, the rich-oxidation state of manganese oxide makes it fit for electrocatalytic reduction reactions in alkaline medium [3]. Thus, based on the logical factors explained above, we successfully developed MnO_2/g-C_3N_4 catalyst with pre-assumed broader characteristics features. The catalyst developed herein has been used for multiple catalysis systems such as, in heterogeneous catalytic reactions for the catalytic reduction of 4-nitrophenol (4-NP) to 4-aminophenol (4-AP) and hydrogenation of styrene to ethylbenzene; in photocatalysis for the degradation of organic pollutant, commercial dye methylene blue (MB) and in electrocatalysis for sustainable energy conversion system with oxygen reduction reactions (ORR) through electro-reduction of oxygen. The broad spectrum featured MnO_2/g-C_3N_4 material has been proved as a catalyst with enhanced performance in multi-catalytic avenues because of its logical state-of-the-art chemistry synchronized with specifically selected applications.

2. Experimental

2.1. Materials

Melamine, cyanuric acid, $MnCl_2$, NaOH, styrene, 4-nitrophenol (4-NP), $NaBH_4$, $HClO_4$ and methylene blue (MB) dye were purchased from Sigma Aldrich. All reagents were used directly without further purification.

2.2. Characterizations

Transmission electron microscopic (TEM) images and high-resolution Transmission electron microscopic (HRTEM) images were taken on a JEM-2100F field emission electron microscope at an accelerating voltage of 200 kV. The high-angle annular dark-field scanning transmission electron microscopy (HAADF-STEM) image and EDS mapping images were taken on a JEOL JEM-ARM200F atomic resolution analytical microscope. The X-ray powder diffraction (XRD) patterns of the products were made on a Philips X'Pert Pro Super diffractometer with Cu-Kα radiation (λ = 1.54178 Å). The operation voltage was maintained at 40 kV and 200 mA current, respectively. A Shimadzu spectrophotometer (Model 2501 PC) was used to record the UV–vis diffuse reflectance spectra of the samples in the region of 200 to 800 nm. The Fourier transform infrared (FTIR) spectra of catalysts were collected using an attenuated total reflection ATR FT-IR Spectrometer Frontier (Perkin Elmer, Waltham, MA, USA). X-ray photoelectron spectroscopy (XPS) measurements were carried out using SPeCS system (PHOIBOS 150, Germany) with Al Kα radiation (hυ¼ 1486.6 eV).

2.3. Synthesis of MnO_2/g-C_3N_4 catalyst

MnO_2/g-C_3N_4 material was synthesized following a facile single-step process of pyrolysis. Melamine and cyanuric acid were chosen as carbon and nitrogen sources and $MnCl_2$ was taken as MnO_2 source. Initially, 0.52 g of melamine, 0.32 g of cyanuric acid, 1 g of $MnCl_2$ and NaOH were added to 50 mL Mili-Q water. This solution mixture was then heated up to 80 °C for 2 h with continuous stirring. Afterwards, the mixture was centrifuged and the residue was dried at 60 °C in a vacuum oven for 12 h. Then, the dried powder was calcined at 550 °C under N_2 environment. After pyrolysis, the material obtained was named as MnO_2/g-C_3N_4 catalyst. For the comparative study, g-C_3N_4 was fabricated using the same procedure without $MnCl_2$ and NaOH in the solution. The schematic diagram of the catalyst synthesis route is shown in Scheme 1, including the final synthesized catalyst material with its two different proposed views, i-e diagonal and cross-sectional views of MnO_2/g-C_3N_4 catalyst.

2.4. 4-Nitrophenol reduction study

The catalytic reduction of 4-NP was carried out using $NaBH_4$ as a reducing reagent. Typically, 1.0 mL of catalyst (1.0 mg/mL) and 8 mL of freshly prepared $NaBH_4$ solution (0.1 M) were sequentially added to 60 μL of 4-NP aqueous solution (10 mM) under magnetic stirring at 30 °C. The UV–visible absorption of the mixture was monitored at regular intervals with a Cary Bio-100 UV/vis spectrometer (Varian).

2.5. Styrene hydrogenation study

Hydrogenation reactions were carried out in hydrogen atmosphere at 35 °C. Typically, styrene (5 mmol), absolute ethanol (10 mL), 1,3,5-trimethylbenzene as internal standard and 4 mg of catalyst were poured into a round-bottom flask. The flask was covered with hydrogen filled balloon. The mixture was stirred at a constant stirring speed for an appropriate time under hydrogen atmosphere. The conversion was determined by GC analysis (GC–MS, Trio-2000, Micromass, U.K).

## 2.6. Methylene blue (MB) degradation study

The degradation experiment was carried out by stirring 10 mL of the mixed aqueous solution of MB (6.25 mg/L) and MnO_2/g-C_3N_4 catalyst nanocomposite (0.14 mmol/L). The solution of MB was separated from the suspension by centrifugation at 8000 r/min for 2 min. Then 1 mL of the supernatant was taken out at certain time intervals and the concentration of MB was monitored by the UV–vis (ultraviolet–visible) spectra of the supernatant of the mixture at the wavelength of 664 nm (using *SEC* 2000-UV/VIS Spectrometer).

2.7. Oxygen reduction reaction study

Before each electrochemical experiment, a glassy carbon (GC) electrode (0.196 cm^2 geometric surface area) was first polished with alumina slurries (Al_2O_3, 0.05 mm) on a polishing cloth to obtain a mirror finish. To prepare a catalyst coated working electrode, 15 μL of the 1 mg/mL sample (MnO_2/g-C_3N_4) suspension in pure water was drop-coated on the polished electrode surface by a microliter syringe. Then, it was dried in a vacuum at room temperature. Afterward, the catalyst was covered with a thin layer of Nafion (0.1 wt% in water, 5 μL) to ensure that the catalyst was tightly attached to the electrode surface during the electrochemical measurements. Voltammetry measurements were carried out with a CHI750D electrochemical workstation. The electrode prepared above was used as the working electrode. The Ag/AgCl (in 3M NaCl, aq.) combination isolated in a double junction chamber, and a Pt coil were used as the reference and counter electrodes, respectively. All the measurements were performed in electrochemical experiments with respect to the standard values of the reversible hydrogen electrode (RHE). Electrochemical experimental work was done by potential cycling method. The electrocatalytic oxygen reduction reactions (ORR) on the catalyst was measured in 0.1 M KOH as the electrolyte by using linear sweep voltammetry (LSV) at a scan rate of 10 mV/s in oxygen environment, and different rotations from 400 rpm to 2000 rpm.

3. Results and discussion

We successfully developed a noble metal-free catalyst containing overlapped MnO_2 and g-C_3N_4 nanosheets to form MnO_2/g-C_3N_4
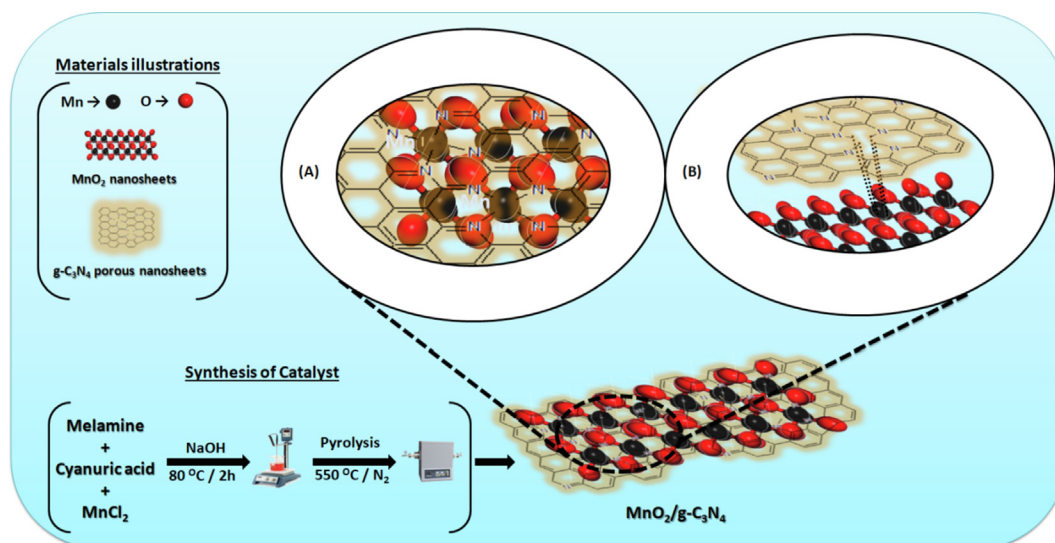
Scheme 1. Synthesis route of the catalyst material, the schematic diagram with insets zoom views of synthesized catalyst **(A)** diagonal view of synthesized MnO_2/g-C_3N_4 **(B)** cross sectional view of material showing Mn is associated with –N sites of g-C_3N_4 in MnO_2/g-C_3N_4 material to evolve Mn—N—C channels.

catalyst. Both nanosheets were combined together by developing strong interactions between metal oxide component and nitrogen of g-C_3N_4. This was done by generating a highly polarized interface within the nanocomposite material. It is highly demanded to provide strong proofs to support these claims by physical characterizations. In order to prove that the materials were synthesized, the characterizations scheme was followed in a bottom-up approach i-e starting from morphological, crystallite structure and ending up with nanocomposite formation confirmation.

To investigate the chemistry of the materials, their morphology and structures were confirmed by scanning electron microscopy (SEM), transmission electrons microscopy (TEM) and high-resolution transmission electrons microscopy (HRTEM). These studies provide clear evidence that the materials were successfully synthesized. The SEM micrographs were taken at two different magnifications as shown in **Figure S1**. As the MnO_2 nanosheets were wrapped up in a g-C_3N_4 layered fluffy/porous material only the upper layer of g-C_3N_4 was shown, as expected with SEM analysis. To further investigate the structural features of the catalyst material, TEM and HRTEM analysis was done. The low and high-magnification TEM analysis shows the morphology of MnO_2/g-C_3N_4 material as MnO_2 nanosheets was covered up with porous g-C_3N_4 sheets like material (Fig. 1**A and 1B**); it has an average crystallite size of 43 nm ± 2 nm. The highlighted red dotted areas of MnO_2 and g-C_3N_4 both depict that the darker metallic sheets of

MnO_2 were fixed in a cloudy porous-like g-C_3N_4 material. To confirm the intimate connection between MnO_2, g-C_3N_4 material and lattice, HRTEM analysis was conducted. The HRTEM analysis has shown clearly that g-C_3N_4 layers are strongly interconnected with the lattice fringes of MnO_2. This suggests there is the formation of interface between MnO_2 and g-C_3N_4, as presented in Fig. 1C. Furthermore, the HRTEM micrograph was used to calculate the lattice fringes for the metallic oxide (MnO_2) nanosheets, which gave the value of *d*-spacing, with 0.24 nm corresponding to the (3 2 1) plane of MnO_2 [26].

The crystalline nature of MnO_2 nanosheets was also confirmed by taking selected area electron diffraction (SAED) image to observe the lattice fringes of MnO_2, as shown in **inset** Fig. 1**D**. These findings together with the apparent morphological and structural analysis proved that MnO_2/g-C_3N_4 nanocomposite material was successfully synthesized. Though the nominal boundaries of MnO_2 nanosheets were drawn by imaginary dotted lines in the figures presented above, the actual sheet-like structure of MnO_2 was also confirmed by HAADF-STEM elemental mappings technique. In Fig. 1**E-1H**, the overlay of elemental mapping image confirmed the proper sheet-like structure of MnO_2 visually. The individual elemental scans of Mn (Ka) and O (Ka) also confirmed that Mn and O were uniformly dispersed in MnO_2 sheets and there was a balanced number of atoms with strong signals of oxygen compared to the manganese with MnO_2 structure.
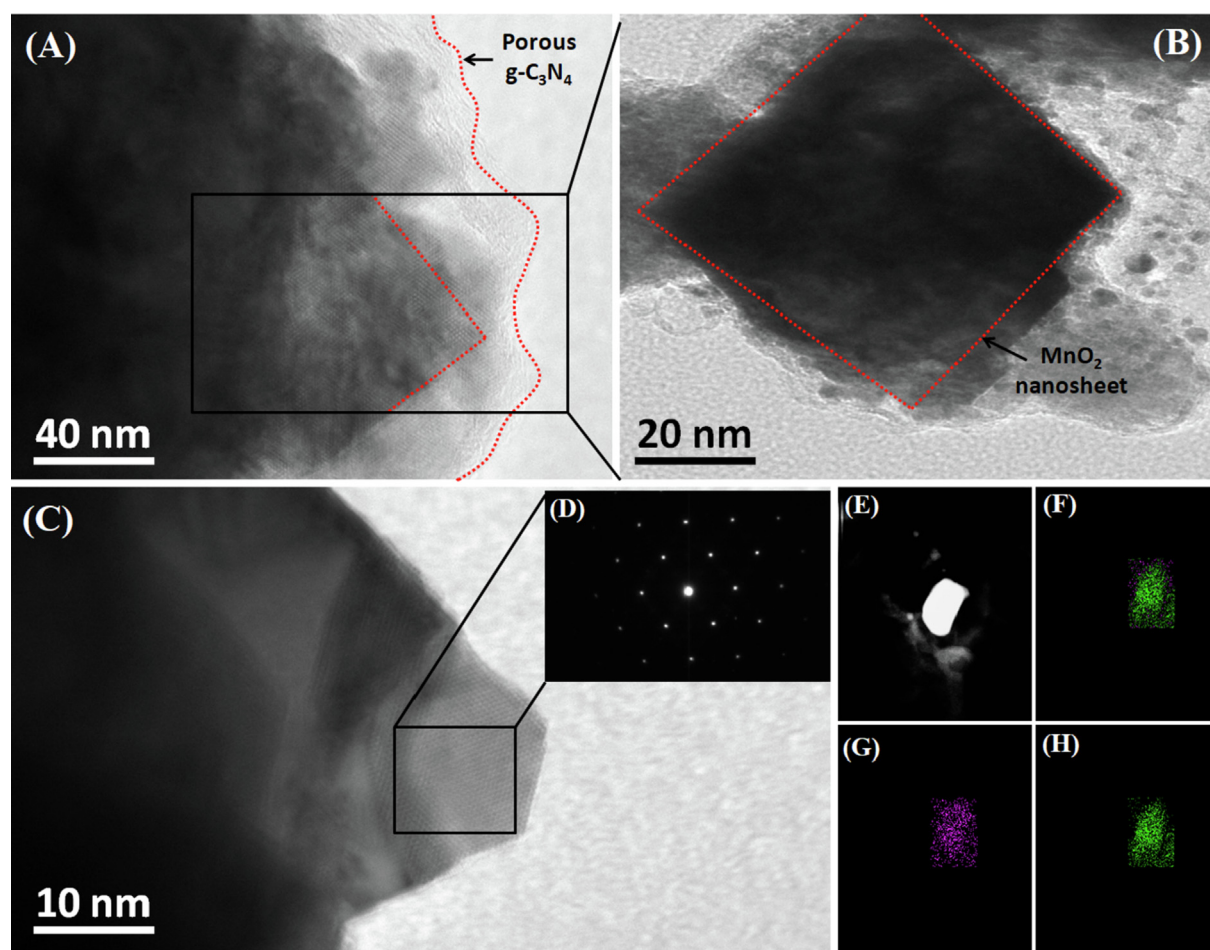

Fig. 1. **Morphological Analysis of MnO_2/g-C_3N_4 nanocomposite: (A) & (B)** TEM images taken at low and high magnifications, respectively, with red dotted lines representing two distinct components i-e porous g-C_3N_4 and MnO_2 nanosheets in MnO_2/g-C_3N_4, **(C)** HRTEM image for MnO_2/g-C_3N_4 nanocomposite with calculated lattice fringes, **(D)** corresponding selected area electron diffraction (SAED) pattern for MnO_2/g-C_3N_4 nanocomposite, **(E)** selected corresponding MnO_2 nanosheets components from MnO_2/g-C_3N_4 nanocomposite for elemental mapping analysis, **(F)** overlay of Mn and O element mapping spots taken from MnO_2 nanosheets, **(G) & (H)** HAADF-STEM element mapping images for Mn and O, respectively, showing the morphology of sheets-like structures.

The powder XRD analysis was done further to evaluate the structural and crystalline phases of MnO_2/g-C_3N_4 nanocomposite material (Fig. 2A). The XRD results showed that the individual g-C_3N_4 scan had a characteristic broad peak that corresponded to the inter layer aromatic stacking of graphitic lattices indexed at 26.04°; it correlated with (002) planes of g-C_3N_4. [27,28] After MnO_2 was added with g-C_3N_4, the XRD scan showed projected characteristics peaks for MnO_2 which closely matched and agreed with the standard (JCPDS No. 44–0141) of pure MnO_2 crystalline phases. The major peaks indexed at 35.24°, 40.45°, 58.81° corresponded to the (210), (211) and (212) planes of MnO_2 crystallites, respectively. [29] Along with MnO_2 lattice peaks, the previously (002) plane peak of g-C_3N_4 at 26.04° was also observed in MnO_2/g-C_3N_4 structure; it had reduced peak intensity due to the overlapping and intimate contact of the metallic oxide (MnO_2) nanosheets. The XRD results obtained for the structural and crystalline phases are in close agreement with HRTEM analysis as well. The overall findings herein depict the interactions and coordination of MnO_2 and g-C_3N_4 through lattice confinements. There are mutual electron transfer channels via interface formation within the nanocomposite material. To further support the presence of functional groups of g-C_3N_4 and the association of metallic oxide (MnO_2) with them, FTIR analysis was performed. In Fig. 2B, the characteristic stretching vibration bond peaks between 1200 and 1600 cm^{-1} corresponded to the C—N bonds, [30] whereas the absorption peaks between 3100 and 3400 cm^{-1} may be attributed to the vibration of acidic hydrogen from amino and hydroxyl groups adsorbed on the surface. [31] The lowered transmittance values observed in MnO_2/g-C_3N_4 spectra at all corresponding peak areas suggest there is the formation of composite structure with mutual associations between the intra-composite components.

The UV/vis diffuse reflectance spectra (DRS) for g-C_3N_4 and MnO_2/g-C_3N_4 nanocomposites were also recorded to analyze their optical properties and to confirm the synthesis of the materials. The absorption edge of g-C_3N_4 and MnO_2/g-C_3N_4 nanocomposite was at 370 nm and 520 nm, respectively, as shown in Fig. 2C. This can be clearly evaluated from the optical behaviour of the nanocomposite compared to g-C_3N_4 material in which optical absorption was remarkable enhanced, resulting in the featured peak shifting towards visible-light region. This redshift in optical absorption features strongly suggests the successful formation of MnO_2/g-C_3N_4 nanocomposite with overlay confinements in which g-C_3N_4 porous sheets-like structure was coupled well with MnO_2 nanosheets.

In line with the structural analysis of MnO_2/g-C_3N_4 nanocomposite, the XPS studies were also carried out to better understand the presence of each element with their appropriate oxidation states and bonding configuration within the nanocomposite material. The XPS full-survey scan confirmed that Mn, O, C and N elements were present in MnO_2/g-C_3N_4 nanocomposite ascribed to the well-documented bonding energies location. To determine the major evolution in MnO_2/g-C_3N_4 after combining both components, the comparison of XPS survey was provided, as shown in Fig. 2D. The number of changes can be clearly observed between these two XPS scans with additional features appearing in MnO_2/g-C_3N_4 compared to g-C_3N_4 material. The following differences
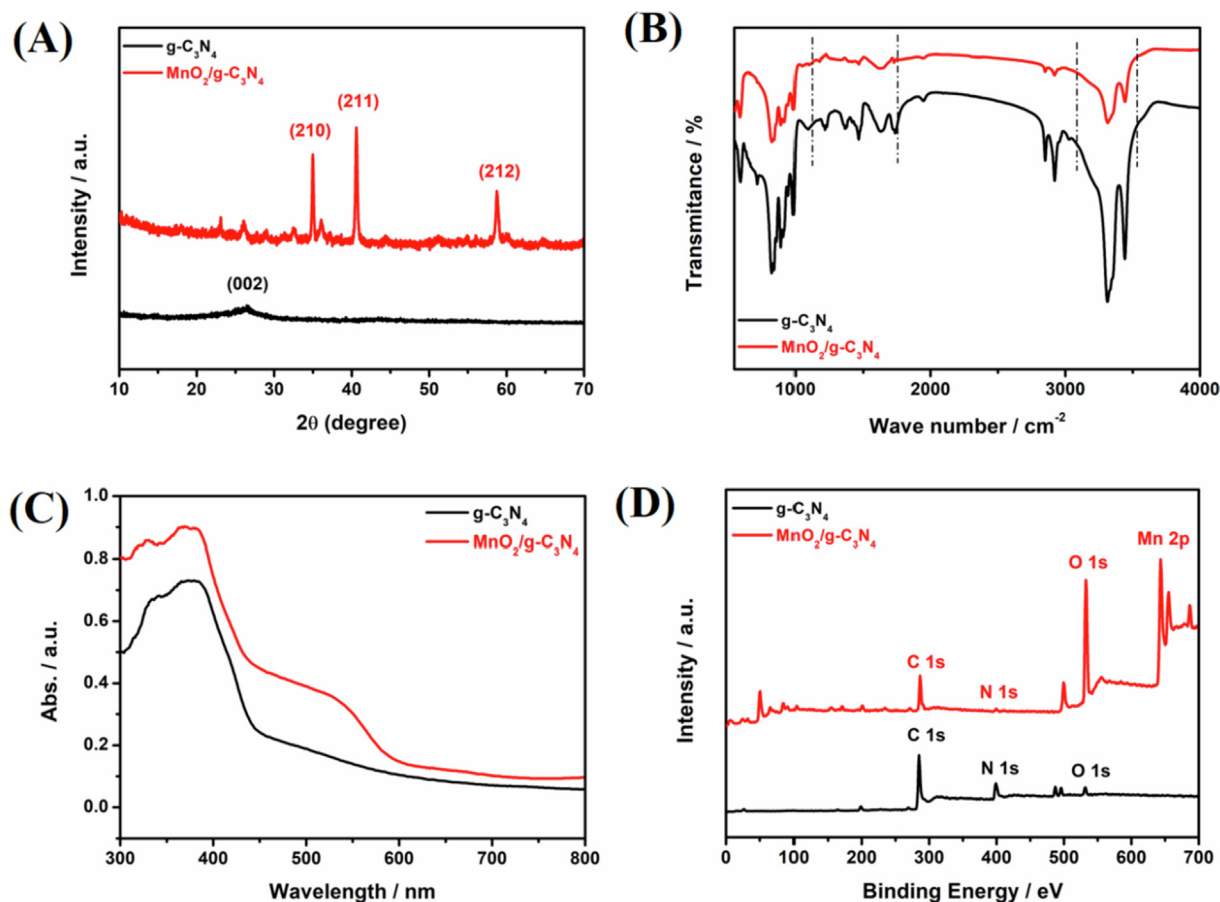

Fig. 2. **Structural Analysis of MnO_2/g-C_3N_4 nanocomposite:** (A) X-ray diffraction (XRD) spectra for g-C_3N_4 and MnO_2/g-C_3N_4, (B) FTIR spectra for g-C_3N_4 and MnO_2/g-C_3N_4, (C) UV–visible diffuse reflectance spectra for g-C_3N_4 and MnO_2/g-C_3N_4, (D) X-ray photoelectron spectroscopy (XPS) spectra of full survey scan taken for both g-C_3N_4 and MnO_2/g-C_3N_4 materials.

can be elucidated between the scans of g-C$_3$N$_4$ and MnO$_2$/g-C$_3$N$_4$ materials: (i) there is a peak area ascribed to Mn, (ii) there is an intense O1s peak in MnO$_2$/g-C$_3$N$_4$ composite, suggesting the presence of lattice oxygen from the metallic oxide (MnO$_2$) component of the nanocomposite along with the surface adsorbed oxygen, which was also shown as minor peak area in g-C$_3$N$_4$scan, (iii) there is a major shift in N1s peak area towards higher binding energy values from g-C$_3$N$_4$ to MnO$_2$/g-C$_3$N$_4$ material (Fig. 2D), suggesting the generation of heterojunction from MnO$_2$ and g-C$_3$N$_4$ during their fabrication. In addition, the higher intensity of N1s peak area was reduced in the later composite material due to the bonding of –N sites of g-C$_3$N$_4$ with the metallic oxide (Mn O$_2$), as proposed [32,34].

The C1s peak in g-C$_3$N$_4$ and MnO$_2$/g-C$_3$N$_4$ corresponded to the graphitic nature of the material indexed at 285.4 eV and 285.7 eV, respectively. It mainly showed an upshift from pristine graphitic peak originally at 284.5 eV, depicting the presence of nitrogen with graphitic carbon in g-C$_3$N$_4$ type material. Furthermore, in XPS analysis, the individual high-resolution spectra for all the elements also provided useful information. The C1s high-resolution spectra (shown in Fig. 3A) had three domains: C—C (at 284.6 eV), C—O/N (at 286.4 eV) and C=N (at 287.6 eV) functional groups [32,35]. The high resolution N1s spectrum (Fig. 3B) retains the characteristic areas for the *sp*2-hybridized nitrogen (C=N–C) at 398.4 eV, bridging nitrogen ((C)$_3$–N) at 399.5 eV and N—H bonding functionality (which replaces the carbon in graphitic framework) at 401.3 eV in g-C$_3$N$_4$ network. [36,37] Among these three

domains, the first two typically known as pyridinic and pyrrolic functionalities of nitrogen also have the lone-pair electron that can serve as metal-coordination sites in MnO$_2$/g-C$_3$N$_4$ to form the interfaces. The upshift in the nitrogen peak of MnO$_2$/g-C$_3$N$_4$ compared to g-C$_3$N$_4$ was ascribed to the pyridinic functionality area. This confirmed the formation of heterojunction and coordination between the metallic oxide (MnO$_2$) sites with –N of g-C$_3$N$_4$.

The high-resolution O1s spectrum in MnO$_2$/g-C$_3$N$_4$ nanocomposite retains features of lattice oxygen at 529.7 eV and surface adsorbed oxygen at 531.6 eV with characteristic bonding functionalities of Mn-O and O—H, respectively (Fig. 3C). [33,38] The lattice oxygen proportion is responsible for the synthesis of metallic oxide species from MnO$_2$ in MnO$_2$/g-C$_3$N$_4$ nanocomposite. It was significantly absent in g-C$_3$N$_4$ whose small peak proportion was only associated with adsorbed oxygen species and other impurities of oxygen. The high-resolution Mn 2p spectrum (Fig. 3D) may also be divided into two domains: Mn 2p$_{1/2}$ and Mn 2p$_{3/2}$. Mn2p$_{3/2}$ can further be deconvoluted into two peak areas associated with the Mn^{4+} oxidation state at 641.7 eV and Mn^{3+} state at 640.6 eV binding energies [39,40]. The peak area corresponds to Mn^{4+}valent state, which quantitatively predominates the competing oxidation state. These features suggest the formation of MnO$_2$ metal oxide species in MnO$_2$/g-C$_3$N$_4$ nanocomposite mainly with (IV) oxidation state. The counter valent proportion was present in minimal unstable proportion, which helped the material to switch the structural rearrangements for the catalyst in multicatalytic fields.
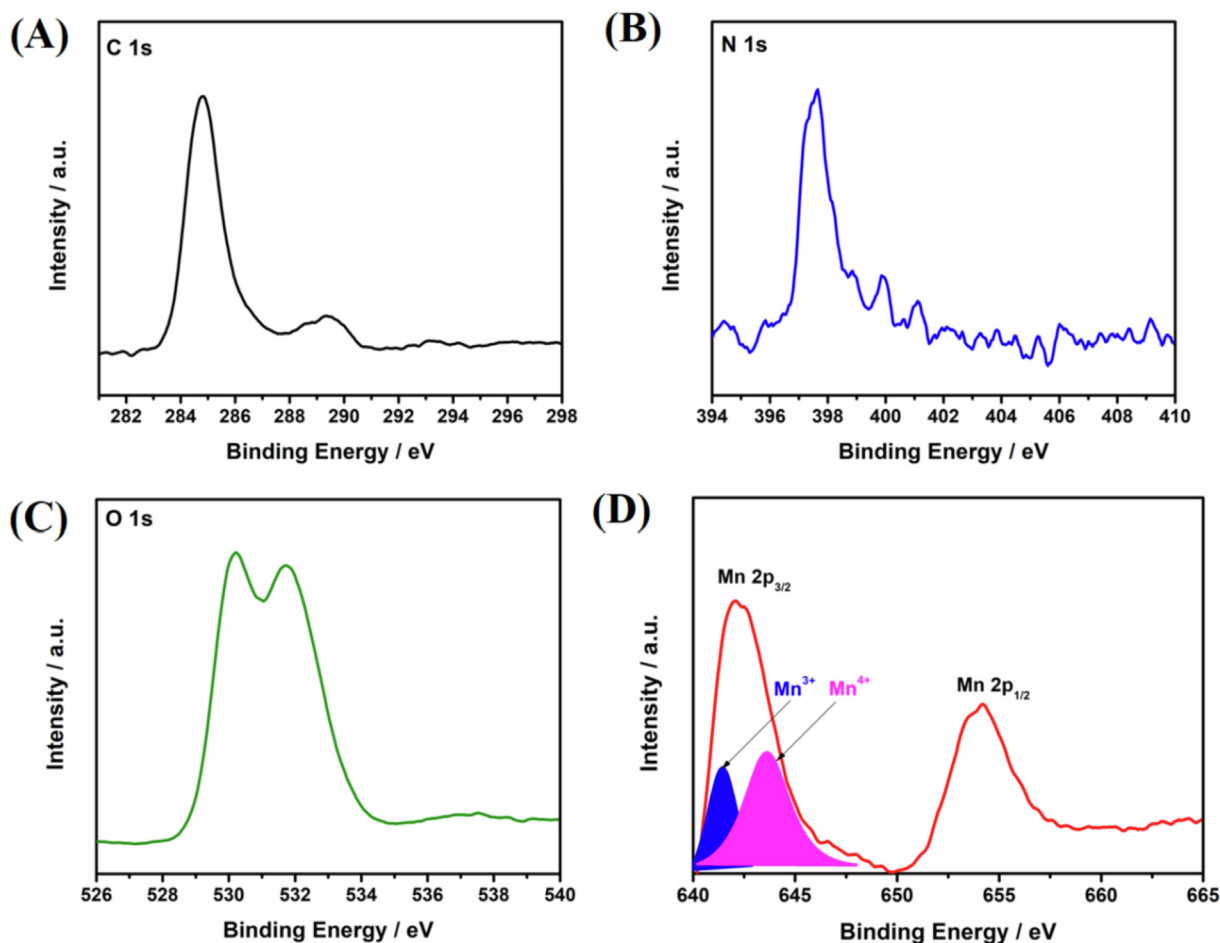

Fig. 3. High resolution XPS scans for individual elements for MnO$_2$/g-C$_3$N$_4$ nanocomposite: **(A)** C 1 s scan, **(B)** N 1 s scan, **(C)** O 1 s scan and **(D)**Mn 2p scan.

3.1. Heterogeneous catalysis study

The ability of the catalyst to involve in heterogeneous reactions was tested by two important processes: the reduction of 4-nitrophenol (4-NP) into 4-aminophenol (4-AP) and the hydrogenation of styrene into ethylbenzene. The catalyst prepared showed remarkable performance in both types of reactions. Heterogeneous reactions require the binding of aromatic compounds with the final product by subsequent catalytic process. The as-developed MnO_2/g-C_3N_4 reduction catalyst can fulfill these basic requirements due to the synergistic association between the two components within the composite material. The reduction catalyst can function individually in both reaction scans due to the multiple synergistic phenomena occurring in it. In addition, due to the environmental and economic challenges facing the developing societies, the noble metal-free catalyst with satisfactory performance has been developed herein. It is comparable with noble metal-based catalysts published in past research works.

3.2. Nitrobenzene reduction

While looking at the geometrical structure of MnO_2/g-C_3N_4, it can be found that both components in this composite material have strong coordinated covalent bond via the –N sites of g-C_3N_4 structure with MnO_2. Whereas, the nitrogen itself known as electronegative specie via the –N sites contains lone-pair electrons. It can be strongly assumed that the interfaces of MnO_2 with nitrogen atoms of g-C_3N_4 effectively activated the Mn-based catalyst to form the catalytically active Mn hydride species with *in-situ* intra-composite electrons migration from g-C_3N_4 to MnO_2. This provided abundant favourable active sites for the adsorption of the substrate to be reduced, thus accelerating the occurrence of the reactions. [41,42] This *in-situ* intra-composite electrons migration is made possible by electron-rich vicinity interface containing electron donor (–N) sites within the MnO_2/g-C_3N_4 nanocomposite. [43] These intra-composite synergistic associations at the interfaces of MnO_2/g-C_3N_4 catalyst made it to be involved in these heterogeneous reactions.

As it is believed that the Langmuir-Hinshelwood model is used for reduction reactions, [43] the catalyst surface acts as a scaffold for adsorbing the substrate and generating a feasible environment for reduction reaction to happen. It enables the substrate to extract hydrogen molecules in the vicinity from the reductant, where it is converted to the final product. The easy adsorption and desorption of the substrate enhances the activity of the catalyst. As the electrons migrate, the g-C_3N_4 part becomes positively charged and the MnO_2 part becomes negatively charged at the interface. [44] The negatively charged vicinity makes the substrate molecules to be reduced during the reactions. This helps to provide hydrogen atoms to facilitate the reduction process. Such a phenomenon creates a number of active sites for the substrate to be adsorbed and reduced. The above synergistic associations and mechanism on the interfaces of the coordinated covalently bounded MnO_2 and g-C_3N_4 through the –N sites and electrons migration process at MnO_2/g-C_3N_4 interfaces strongly support that Langmuir-Hinshelwood model is used for reduction. These claims may provide a fair and state-of-the-art mechanistic theme of enhanced reaction on this non-precious metal MnO_2/g-C_3N_4 catalyst.

In the present work, the first heterogeneous hydrogenation reaction was studied with catalytic reaction model, in which there was the catalytic reduction of 4-NP into 4-AP in the presence of $NaBH_4$. It is more convenient to monitor its kinetics with a spectrophotometer. The catalytic reaction is typically preceded in an aqueous medium with a specified frame of induction period for it to be stalled properly. This was followed by the reconstruction of the catalyst surface for it to become activated. The benchmark reaction was initiated where the substrate molecules-immobilized nanostructures were aligned facing the four-sided walls of a cuvette. These geometries of reactants and the products produced against the walls allow the laser beam to pass through the reactants and products (adsorbed and desorbed molecules) from the activated immobilized nanostructures. In this way, the probe beam cannot be compromised or interfered with plasmonic nanoparticles interactions while testing the results.

In doing so, with a typical model of reaction the initially observed characteristic 4-NP absorption peak gradually decreased by increasing the 4-AP peak absorbance area, as shown in **Figure S2**. The success with the state-of-the-art mechanism of reduction reaction in the catalyst has already been discussed in the above paragraphs. The basic scientific logic of the reaction can be explained in a way that the reaction contains dissolved sodium borohydride, MnO_2/g-C_3N_4 and the 4-NP molecules. The dissociation of sodium borohydride in aqueous medium produces the borohydride ions that react with the surface of MnO_2 for the reconstruction of immobilized nanostructure active sites. These active sites adsorb the substrate molecules and transfer the surface hydrogen atoms via the hydride (Mn hydride) species produced by the phenomenon of electrons transfer from g-C_3N_4 to MnO_2 at the interface. The sequential process starts with the reduction of nitrophenol: at first, nitrophenolate is converted into nitroso compounds, then it is reduced to hydroxylamine compounds and finally converted into aminophenolate.

The UV–vis spectrometry shows that the characteristic peak of pristine 4-NP is observed at 317 nm with its light yellow colour. This peak abruptly shifted at 400 nm after the addition of $NaBH_4$ and also after the light yellow colour changed to bright yellow due to the formation of phenolate ion of 4-NP solution with dissociated borohydride ions [45]. The colour of the solution did not change after 30 min, as well as the peak position. This suggests that reduction reaction cannot be done by only $NaBH_4$ with 4-NP. Thereafter, the MnO_2/g-C_3N_4 catalyst was added to the alkaline 4-NP solution. Then, the reduction reaction started following dip catalyst modality. It was clearly observed that the peak hump of 4-NP at 400 nm gradually decreased; thus, a new peak appeared which was positioned at 298 nm corresponding to 4-AP production. According to the spectrophotometeric results obtained, the prior peak at 400 nm completely disappeared after 6 min due to increased new peak area at 298 nm and the solution became colourless. This shows there was a complete catalytic reduction of the nitro-group (–NO_2) of 4-nitrophenolate into the amino-group (–NH_2) of 4-aminophenolate (Fig. 4**A**).

In contrast, the comparative study was also done for g-C_3N_4 catalyst to understand the specific role of MnO_2 with g-C_3N_4 in MnO_2/g-C_3N_4 catalyst. The results for g-C_3N_4 catalyst without MnO_2 component showed that the UV/Vis absorption peak at 400 nm slightly dropped for 30 min, thereafter it remained unchanged. This suggests the incomplete reduction of 4-NP, as shown in Fig. 4**B and Figure S3**. The kinetics of reduction reaction has also been determined in the present studies (Fig. 4C), with measured K value of 0.00624 min^{-1} and 0.734 min^{-1} for g-C_3N_4 and MnO_2/g-C_3N_4 catalysts, respectively. The higher K value obtained compared to the documented noble and non-noble metal-based composite materials suggests the enhanced performance of MnO_2/g-C_3N_4 catalyst for complete reduction of 4-NP into 4-AP, with fast first-order kinetics. Furthermore, the superiority of the present catalyst material (MnO_2/g-C_3N_4) in terms of enhanced 4-NP reduction was comprehensively evaluated and compared with reported catalyst materials in Table S1. The durability of catalysts is a critical factor that determines their performance in catalysis. The as-tested performance of the catalyst was also monitored by repeating the reaction in five cycles following the same protocol. The durability tests presented in Fig. 4**D** proved the stable nature of the reaction after
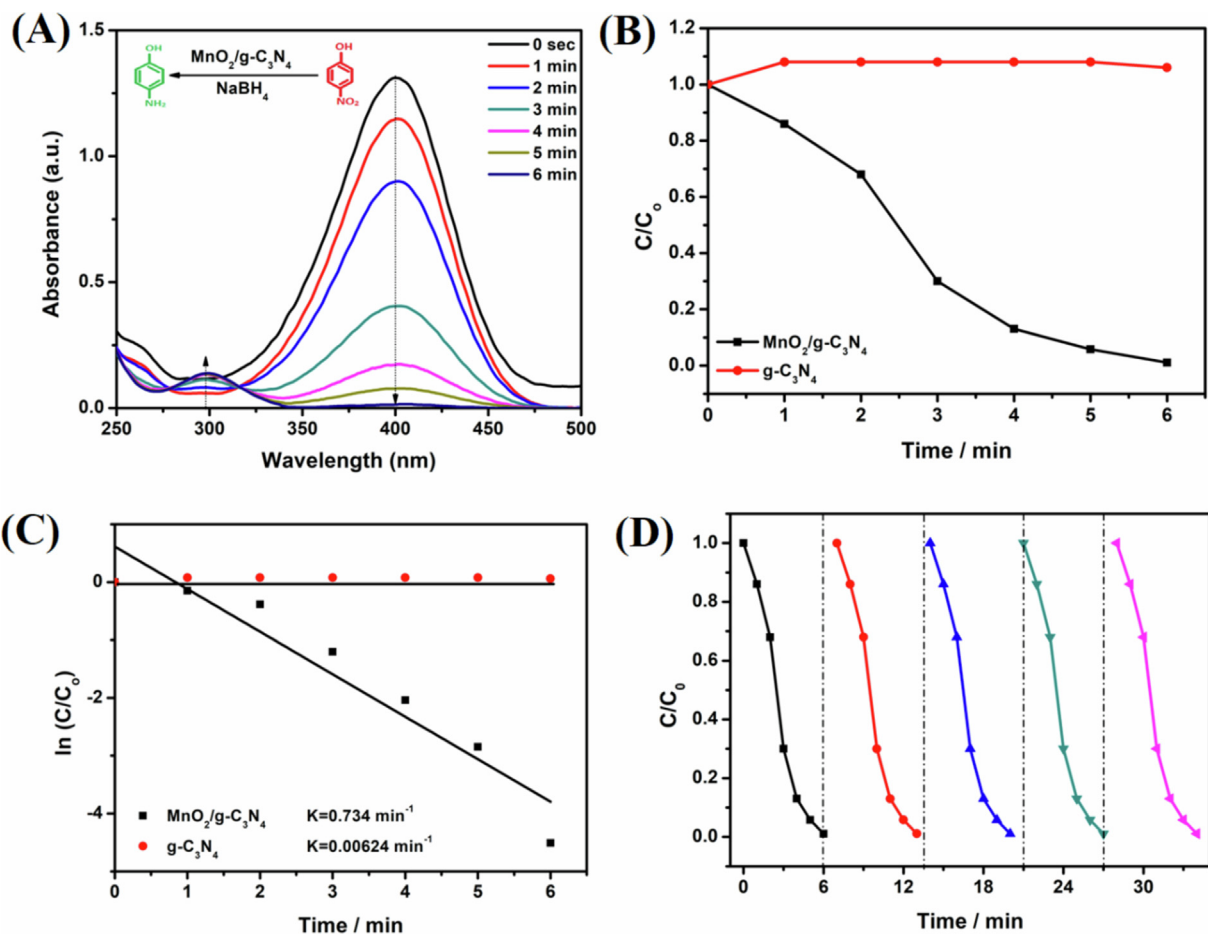
Fig. 4. Heterogeneous catalysis performance for the reduction of 4-nitrophenol into 4-aminophenol:(A) reduction of 4-NP into 4-AP on $MnO_2/g-C_3N_4$ catalyst, **(B)** comparative performance analysis of 4-NP reduction on both $MnO_2/g-C_3N_4$ and $g-C_3N_4$ catalysts, **(C)** calculation of rate constant values for both $MnO_2/g-C_3N_4$ and $g-C_3N_4$ catalysts, **(D)** durability test of 4-NP reduction into 4-AP for $MnO_2/g-C_3N_4$ with various cycles.

consecutively five repeated cycles with no observed loss in the performance of the catalyst.

3.3. Styrene hydrogenation

Furthermore, the hydrogenation of styrene into ethylbenzene has been chosen as a second catalytic reaction model to evaluate the performance of $MnO_2/g-C_3N_4$ catalyst in heterogeneous hydrogenation reactions. Developing a noble metal-free state-of-the-art catalyst for styrene hydrogenation reaction can be a breakthrough study to facilitate important organic conversion reactions in industries. The results obtained have shown the catalytic conversion of styrene into ethylbenzene was completed (100% conversion) in 120 min for $MnO_2/g-C_3N_4$ catalysts, whereas for $g-C_3N_4$ there was only 12% conversion at the same interval of time (Fig. 5**A**). The improved performance of MnO_2 in $g-C_3N_4$ material can be ascribed to the high electron density due to the delocalized electrons at the interface of MnO_2 and $g-C_3N_4$ within $MnO_2/g-C_3N_4$ catalyst. Moreover, the effect of the reactants' concentrations has also been observed with three different amounts of styrene to obtain the optimal concentration of styrene for successful conversion (Fig. 5**B**).

The basic heterogeneous hydrogenation mechanism in the present material has been explained in depth in this study. But more specifically, the surface mechanism can be designed and explained with strong convincing proofs as follows: In the Langmuir–Hinshelwood model, hydrogen is dissociatively chemisorbed [46,47], while in the Horiuti–Polanyi model, the heterogeneous hydrogenation reaction follows three basic steps reaction. The first is the adsorption of styrene (substrate) compound on the hydrogenated metal surface of the catalyst; the second is the migration of hydrogen to the beta-carbon of the styrene by generating delta-bond between the alpha-carbon and the metal active site called semi-hydrogenated intermediate species; the third is the reductive elimination or desorption of the free ethylbenzene. [48]

In $MnO_2/g-C_3N_4$ catalyst the highly delocalized electrons at the interface increase the donor density and favor the adsorption of styrene and hydrogen. Thus, they also reduce the energy barriers for cleavage of bonds to initiate the catalysis reaction. This can be assumed in the current reaction that hydrogen and styrene compete for the same active sites for adsorption on the catalyst surface. Alkene is adsorbed on Mn active sites, where Mn hydride is formed after the structure is reconstructed at the interface by electrons migrating from –N sites of $g-C_3N_4$. This adsorbed alkene compound gained two hydrogen atoms (H_{ads}) step by step from adjacent vicinities. The durability of the reaction is an important factor used to evaluate the profile of the catalyst performance. We also tested the styrene hydrogenation activity of the catalyst in five repeated cycles following the same protocol, as shown in Fig. 5**C**. The reuse of the catalyst after five cycles suggests the durable and stable reaction performance of the catalyst, with no apparent loss in performance.
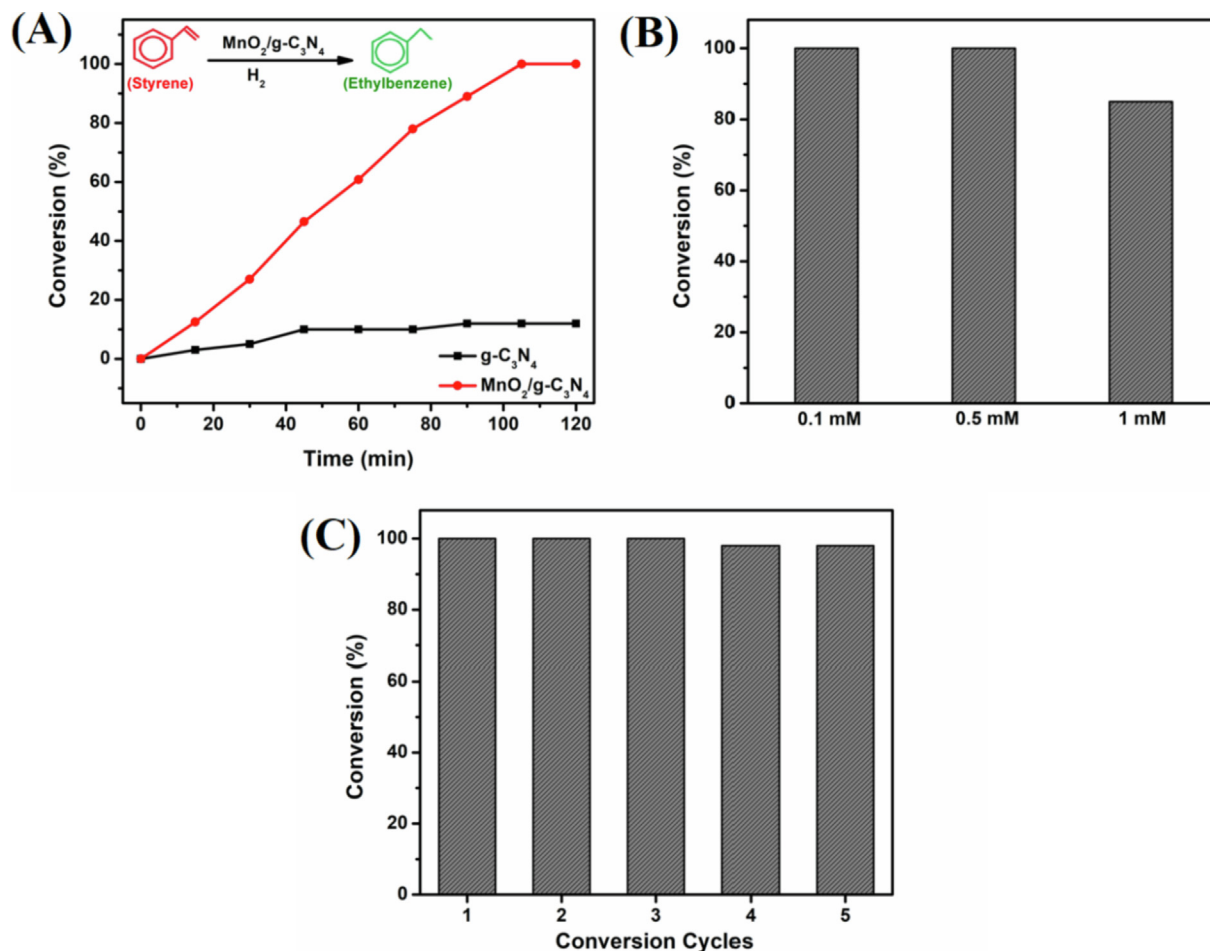
Fig. 5. Heterogeneous hydrogenation catalysis performance for the conversion of styrene into ethylebenzene: (A) Conversion changes over. time for the hydrogenation of styrene for both MnO$_2$/g-C$_3$N$_4$ and g-C$_3$N$_4$ catalysts, **(B)** Conversion changes over. time for the hydrogenation of styrene at different concentration of styrene for MnO$_2$/g-C$_3$N$_4$ catalyst, **(C)** durability and repeatability tests after 5 successive catalytic cycles for MnO$_2$/g-C$_3$N$_4$ catalyst.

3.4. Photo-catalysis study

The photocatalytic performance of MnO$_2$/g-C$_3$N$_4$ catalyst has been examined by photo-degradation of organic pollutant methylene blue (MB) under UV/vis light. The photoresponsive range of these types of nanomaterials becomes narrow due to quantum size effect. This leads to a blue-shifted optical absorption and thus lowers the utilization of solar irradiation. Herein, the testing material falls into this category; thus it is selected for MB degradation because it is a highly efficient material, is environmental friendly, cheap and abundant in nature. The photocatalytic performance of MnO$_2$/g-C$_3$N$_4$ material was also compared with g-C$_3$N$_4$, in order to evaluate the importance of interjection material of MnO$_2$ nanosheets along with g-C$_3$N$_4$ layered porous structure.

The enhanced photocatalytic degradation of MB on MnO$_2$/g-C$_3$N$_4$ can be briefly explained as follows. The nano-sized manganese oxide-based composites may act as adsorbent and degradant of different kinds of organic pollutants and dyes because of its octahedral crystal structure with large surface area and high redox potential. In addition, g-C$_3$N$_4$ has attracted huge attention in photocatalytic applications because its layered structure is similar to graphite and can be exfoliated into nanosheets. Whereas, g-C$_3$N$_4$ layered nanosheets can have increased photocatalytic activities due to their high specific surface area and shortened path length of charge carriers.

It is strongly believed that photocatalysis is a surface phenomenon mainly and is highly sensitive to the surface characteris-

tics of the catalysts being used. [49,50] The results have shown notably 98% of MB degradation within 20 min in the presence of MnO$_2$/g-C$_3$N$_4$ catalyst (Fig. 6**A**). Whereas in comparison, there is no or negligible amount of MB degradation observed in the presence of g-C$_3$N$_4$ catalyst (Fig. 6**B and S4)**. The enhanced and facile MB degradation on MnO$_2$/g-C$_3$N$_4$ catalyst may be ascribed to its exceptional surface features. The enhanced photocatalytic behaviour is due to the two types of mechanisms happening simultaneously in the present catalyst material.

Firstly, the electrostatic charges induced on the surface due to MnO$_2$ and g-C$_3$N$_4$ interfaces accumulate hydroxyl species on the surface. These hydroxyl species on the graphitic-like structure of g-C$_3$N$_4$ favoured the crystal structure of MnO$_2$ facilitating the adsorption of substantial amount of MB molecules. This led to the decomposition of MB in the presence of increasing free radical species ($^\bullet$OH, $^\bullet$O^2), as seen in common MB degradation reactions. [51,52] Secondly, the unique two dimensional interfaces of MnO$_2$ and g-C$_3$N$_4$ overlapped nanosheets generate heterojunction. Thus, charge carrier extraction was enhanced and used during photoexcitation with the help of photo-induced electrons in MnO$_2$ combined with the holes in g-C$_3$N$_4$. [49] These two supported mechanisms in the presence of MnO$_2$/g-C$_3$N$_4$ catalyst enhanced the photocatalytic degradation of MB. The apparent reaction rate constant (*K*) for MnO$_2$/g-C$_3$N$_4$ catalyst was ca. 0.208 min^{-1}, which was much higher than that of g-C$_3$N$_4$ catalyst observed as ca. 0.000982 min^{-1}. The rate constant is seen in Fig. 6**C**. Along with the photo-degradation results, the kinetic interpretations have
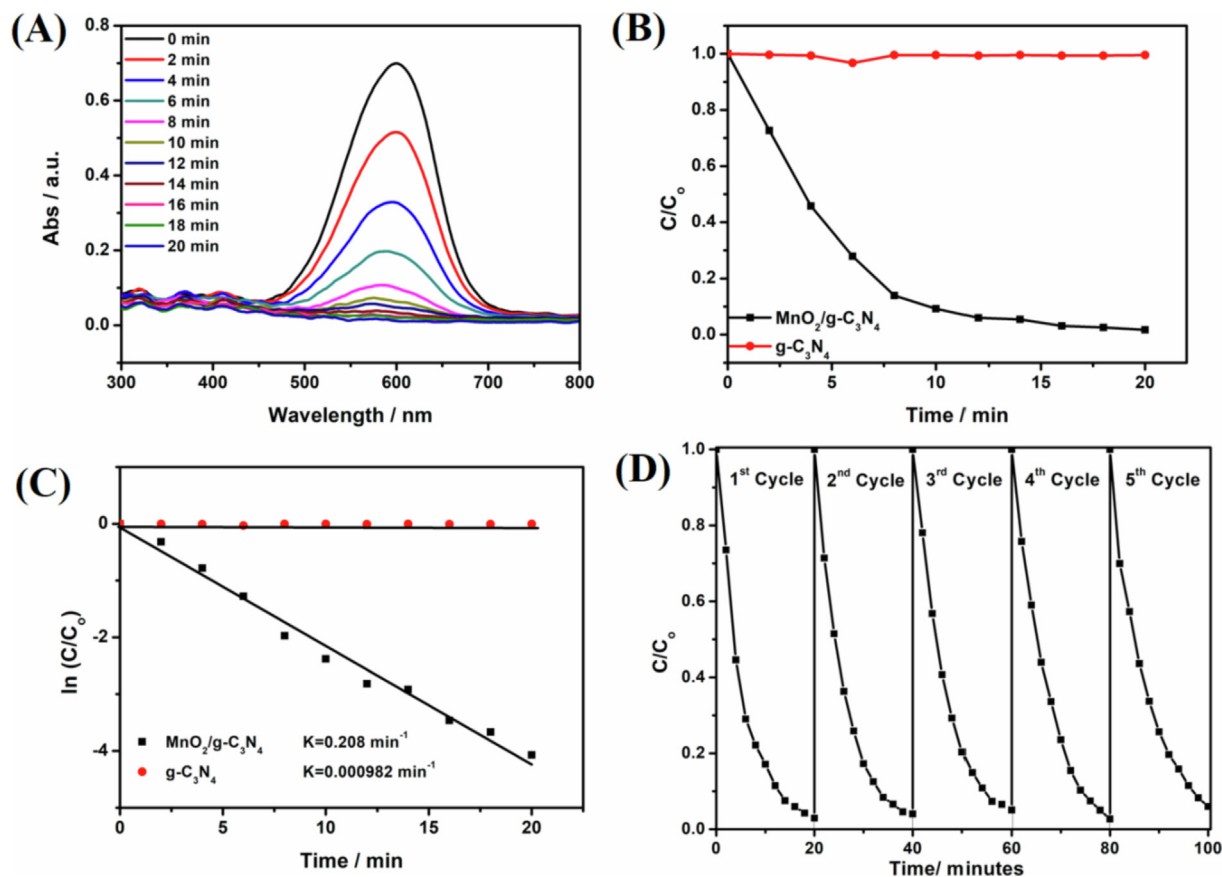
Fig. 6. Photocatalytic performance for methylene blue degradation: (A) Time-dependent de-coloration of MB in the photocatalysis reaction under visible light irradiation for MnO_2/g-C_3N_4 catalyst, **(B)** comparative analysis of MB degradation on both MnO_2/g-C_3N_4 and g-C_3N_4 catalysts, **(C)** calculation of rate constant for both MnO_2/g-C_3N_4 and g-C_3N_4 catalysts with analyzed data, **(D)** durability test of MB degradation with MnO_2/g-C_3N_4 after five consecutive cycles.

shown that reaction obeyed the pseudo-first-order kinetics following Langmuir-Hinshelwood model (Fig. 6**B and 6C**). [49,53] In addition, critical comparison was made between MnO_2/g-C_3N_4 catalyst and other catalysts reported in the literature in relation to the degradation of MB (**Table S2**). It shows the state-of-the-art catalyst material used in this study has exceptionally best performance. The reproducibility of photocatalytic performance is an important factor worth analyzing. It signifies the effectiveness and durability of the material after being consecutively recycled for multiple times. As shown in Fig. 6**D**, the recycled MnO_2/g-C_3N_4 catalyst maintained its activity after five cycles. These results demonstrate the stability of the material.

3.5. Electro-catalysis study

The electrocatalytic performance of MnO_2/g-C_3N_4 catalyst was studied based on the oxygen reduction reactions (ORR) model at the cathodic end of alkaline fuel cells. The electrocatalytic ORR experiments were done with conventional linear sweep voltammetry (LSV) polarization plots. They were done by rotating disk electrode (RDE) setup on the catalyst ink-loaded glassy carbon electrode (GCE) with continuous purging of oxygen in the alkaline medium of 0.1 M KOH. The obtained ORR polarization curves showed typical characteristic reduction current, suggesting successful electro-reduction of oxygen on the catalyst surface (Fig. 7**A**). As expected the values of reduction current increased linearly by increasing the rotation rate of electrode, as shown in Fig. 7**A and 7B**. The ORR polarization curve obtained at the rotation rate of 1600 rpm was also compared with the g-C_3N_4 material and

commercial electrocatalysts used as cathodes for conventional fuel cells such as Pt/C (20 wt%) and Pd/C (20 wt%) (Fig. 7**C and Figure S5**).

The typical characteristic polarization trend for the LSV results obtained at all rotation rates shows three ORR current regions: the kinetic-controlled area (between ca. 1 V to 0.75 V), the diffusion-controlled area (between ca. 0.40 V to 0.20 V) and the mixed kinetic-diffusion controlled area (between ca. 0.75 V to 0.40 V). The exceptional features have been observed in the results obtained with mixed kinetic-diffusion controlled area and subdivision of curve rather than a straight line. This suggests the electro-reduction of oxygen was led by dual accelerating factors due to the interfacial material. The electro-reduction of oxygen started in the kinetic-controlled area and was accelerated by entering into the mixed kinetic-diffusion controlled area after showing the onset potential. The obtained current density increased as the potential dropped and finally gave diffusion limiting current.

The ORR electrocatalysis route may be ascribed to the adsorption and chemisorptions of oxygen molecules on the surface of the catalyst. The MnO_2 based catalyst has superior performance for ORR due to the multivalent features of Mn in the catalyst. The oxidation state of Mn in MnO_2 based material is (IV) which is swathed to other states in electron transfer reactions where the material behaves as reduction catalyst. Due to these structural rearrangements and multivalent features of Mn, it behaves as oxygen buffer to adsorb more oxygen on its surface. The adsorbed oxygen is then chemisorbed into final product by the interactions of nearby HO_2^- species produced at g-C_3N_4 sites [7]. The supportive mechanism in the present material may also be suggested by the
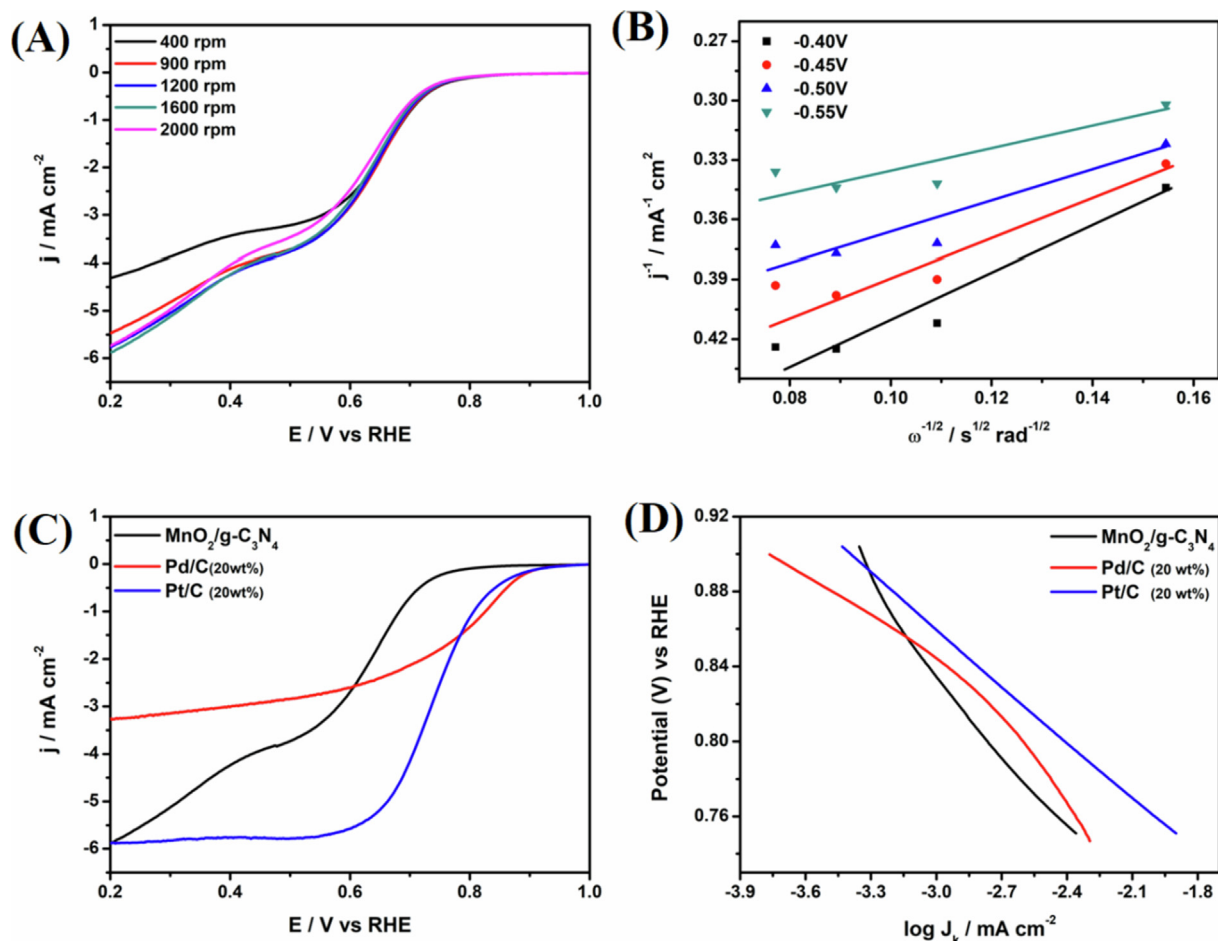
Fig. 7. Electrocatalytic performance for oxygen reduction reactions (ORR): (A) the ORR polarization curves obtained at different rotations in alkaline medium with continuous purging of oxygen for $MnO_2/g\text{-}C_3N_4$ catalyst, **(B)** K-L plots at different potentials vs RHE for $MnO_2/g\text{-}C_3N_4$ catalyst, **(C)** ORR polarization curves obtained at rotation of 1600 rpm for $MnO_2/g\text{-}C_3N_4$ catalyst compared with commercial Pt/C (20 wt%) and Pd/C (20 wt%) catalysts measured at same experimental protocol, **(D)** corresponding Tafel plots of ORR for $MnO_2/g\text{-}C_3N_4$ compared with commercial catalysts.

mixed-adsorption theory given by El-Deab and Ohsaka, where the oxygen molecule is prone to be adsorbed at the interface [54]. This kind of adsorption of oxygen in the catalyst gave higher concentration of available adsorbed oxygen at the active sites of the catalyst compared to the monometallic nanoparticle materials. In the present material the interface between MnO_2 and $g\text{-}C_3N_4$ nanosheets synergistically improved the performance of the catalyst.

The performance of cathode catalyst may be evaluated based on various factors, but more importantly, the onset potential and diffusion limiting current values are considered to be more prestigious sources. Herein, the onset potential of the catalyst was negative compared to the commercial catalysts. This was responsible for the delayed initiation of ORR electrocatalysis on $MnO_2/g\text{-}C_3N_4$ catalyst. This can be compensated with the factor of excessive adsorption of O_2 on the catalyst at the interfacial sites. This adsorption quantitatively delayed the initiation of ORR. However, when the potential decreased the obtained current density values abruptly increased by providing higher diffusion limiting current compared to Pd/C. It was almost comparable with Pt/C catalysts. $MnO_2/g\text{-}C_3N_4$ had higher diffusion current density value than the commercial catalysts. This strongly suggests that $MnO_2/g\text{-}C_3N_4$ material is a superior precious-metal-free catalyst for ORR [55].

Furthermore, the quantitative analysis has been done to evaluate the performance of the present catalyst by Tafel plots and compare it with commercial catalysts (Fig. 7D). The obtained slope value for the catalyst provided the information that the ORR elec-

trocatalysis occurred at the rate that determined the step of the first electron transfer reaction on $MnO_2/g\text{-}C_3N_4$ catalyst [55,56]. The Koutecky − Levich (K − L) plots derived from ORR polarization curves at different rotations further exhibited the electron transfer number (n) during the electro-reduction of oxygen (Fig. 7B). The ORR electrocatalysis by Pt-based and precious metal-based catalyst is led by four and two-electron transfer mechanisms. The lower "n" values correspond to low electrochemical activity of the catalyst. The calculated n value for $MnO_2/g\text{-}C_3N_4$ catalyst was obtained ∼ 4 at a large potential range, suggesting the four electron-pathways for the electro-reduction of oxygen with this catalyst [55,56]. The accelerated durability test (ADTs) for ORR was also done by following the same experimental protocol, as shown in **Figure S6**. The ADTs result showed ∼ 2% of activity loss after 1000 cycles. This is negotiable for the precious metal-free catalyst which has exceptional diffusion current density that can be applied practically in alkaline fuel cells.

4. Conclusions

In concluding the overall stuffed study, we have been successful in developing an exceptional multi-featured catalyst for multi-directional applications in handling environmental and energy challenges. The $MnO_2/g\text{-}C_3N_4$ catalyst was synthesized by pyrolysis method in which the *in-situ* calcined environment generated coordination sites between $g\text{-}C_3N_4$ and MnO_2 components via delocal-

ized π-conjugated system with lone pair of nitrogen atoms and metallic oxide, respectively. This intimate contact between g-C_3N_4 and MnO_2 was successfully confirmed with TEM and HRTEM micrographs by physical characterizations in which the lattice of MnO_2 was intermixed with fluffy-sheet-like g-C_3N_4 network. These coordination sites developed high electron density interfaces acting as active sites for providing electronic pull and synergistic effects in the reconstruction of the internal structure of the catalyst. This provided favourable environment for catalysis to occur successfully. Later on, these were also confirmed by the red shift in the material's optical behaviour in DRS analysis and the shift of nitrogen indexed peak towards higher bonding energies value in XPS analysis, from g-C_3N_4 to MnO_2/g-C_3N_4, respectively. These physicochemical characterization results suggest the formation of active interfaces within MnO_2/g-C_3N_4 catalyst, which may favour their intrinsic role in their optical and electrochemical properties.

The developed catalyst has been used in three major catalysis fields to handle environmental and energy crises. The environmental challenges mainly focussed on the conversion and degradation of organic pollutant species into useful or less harmful species produced as industrial hazardous wastes. Whereas, the energy crisis demands production of clean energy resources from sustainable roadmaps to mitigate the consumption of fossil fuels and greenhouse effect. In this context, the conversion of organic molecules such as 4-NP and styrene into 4-AP and ethylbenzene was done using heterogeneous catalysis approach, the degradation of organic pollutant dye MB was done with photocatalysis technique and electrocatalysis was used for sustainable energy production by electro-reduction of air oxygen molecules. The exceptional behaviour of MnO_2/g-C_3N_4 material proved to be an effective catalyst in multi-directional fields with an enhanced and durable performance.

CRediT authorship contribution statement

Ammar Bin Yousaf: Conceptualization, Formal analysis, Methodology, Data curation, Writing – original draft, Writing – review & editing. **Fatima Sifani Zavahir:** Formal analysis, Investigation, Writing – review & editing. **Akif Zeb:** Formal analysis, Investigation, Writing – review & editing. **Alena Michalcova:** Formal analysis, Writing – review & editing. **Peter Kasak:** Conceptualization, Funding acquisition, Data curation, Writing – review & editing.

Declaration of Competing Interest

The authors declare that they have no known competing financial interests or personal relationships that could have appeared to influence the work reported in this paper.

Acknowledgements

Appendix A. Supplementary material

Supplementary data to this article can be found online at https://doi.org/10.1016/j.jcis.2021.12.023.

References

[1] G. Kyriakou, M.B. Boucher, A.D. Jewell, E.A. Lewis, T.J. Lawton, A.E. Baber, H.L. Tierney, S.M. Flytzani, E.C. Sykes, Isolated metal atom geometries as a strategy for selective heterogeneous hydrogenations, Science 335 (2012) 1209–1212.

[2] F. Wang, S. Song, K. Li, J. Li, J. Pan, S. Yao, X. Ge, J. Feng, X. Wang, H. Zhang, A "solid dual-ions-transformation" route to S, N Co-doped carbon nanotubes as highly efficient "metal-free" catalysts for organic reactions, Adv. Mater. 28 (48) (2016) 10679–10683.

[3] J. Zhang, Y. Li, L. Wang, C. Zhang, H. He, Catalytic oxidation of formaldehyde over manganese oxides with different crystal structures Catal, Sci. Technol. 5 (2015) 2305–2313.

[4] B.C.H. Steele, A. Heinzel, Materials for fuel-cell technologies, Nature 414 (2001) 345–352.

[5] M.K. Debe, Electrocatalyst approaches and challenges for automotive fuel cells, Nature 486 (2012) 43–51.

[6] H.-L. Jiang, Q. Xu, Recent progress in synergistic catalysis over heterometallic nanoparticles, J. Mater. Chem. 21 (36) (2011) 13705.

[7] S. Cao, N. Han, J. Han, Y. Hu, L. Fan, C. Zhou, R. Guo, Mesoporous hybrid shells of carbonized polyaniline/Mn2O3 as non-precious efficient oxygen reduction reaction, ACS Appl. Mater. Interfaces 8 (9) (2016) 6040–6050.

[8] Z. Wu, Y. Xue, H. Wang, Y. Wu, H. Yu, ZnO nanorods/Pt and ZnO nanorods/Ag heteronanostructure arrays with enhanced photocatalytic degradation of dyes, RSC Adv. 4 (2014) 59009–59016.

[9] W. Xia, A. Mahmood, Z. Liang, R. Zou, S. Guo, Earth-abundant nanomaterials for oxygen reduction, Angew. Chem. Int. Ed. 55 (8) (2016) 2650–2676.

[10] Clusters and Colloids, From Theory to Application, ed, VCH, New York, J. S. Bradley and G. Schmid, 1994, p. 459.

[11] N. Porter, H. Wu, Z. Quan, J. Fang, Shape-control and electrocatalytic activity-enhancement of Pt-based bimetallic nanocrystals, Acc. Chem. Res. 46 (2013) 1867–1877.

[12] Z.F. Bian, J. Zhu, J.G. Wang, S.X. Xiao, C. Nuckolls, H.X. Li, Multitemplates for the hierarchical synthesis of diverse inorganic materials, J. Am. Chem. Soc. 134 (2012) 2325–2331.

[13] A.B. Yousaf, M. Imran, A. Zeb, X. Xie, K. Liang, X. Zhou, C.-Z. Yuan, A.-W. Xu, Synergistic effect of graphene and multi-walled carbon nanotubes composite supported Pd nanocubes on enhancing catalytic activity for electro-oxidation of formic acid, Catal. Sci. Technol. 6 (13) (2016) 4794–4801.

[14] Y.-J. Wang, D.P. Wilkinson, J. Zhang, Noncarbon support materials for polymer electrolyte membrane fuel cell electrocatalysts, Chem. Rev. 111 (12) (2011) 7625–7651.

[15] X.J. Wan, Y. Huang, Y.S. Chen, Focusing on energy and optoelectronic applications: a journey for graphene and graphene oxide at large scale, Acc. Chem. Res. 45 (2012) 598–607.

[16] X. Huang, X. Qi, F. Boey, H. Zhang, Graphene-based composites, Chem. Soc. Rev. 41 (2) (2012) 666–686.

[17] Z. Zhao, Y. Sun, F. Dong, Graphitic carbon nitride based nanocomposites: a review, Nanoscale 7 (1) (2015) 15–37.

[18] S. Gu, J. Xie, C.M. Li, Hierarchically porous graphitic carbon nitride: large-scale facile synthesis and its application toward photocatalytic dye degradation, RSC Adv. 4 (2014) 59436–59439.

[19] H. Gao, S. Yan, J. Wang, Y. Huang, P. Wang, Z. Li, Z. Zou, Towards efficient solar hydrogen production by intercalated carbon nitride photocatalyst, Phys. Chem. Chem. Phys. 15 (2013) 18077–18084.

[20] G.M. Veith, L. Baggetto, L.A. Adamczyk, B. Guo, S.S. Brown, X.G. Sun, Electrochemical and solid-state lithiation of graphitic C_3N_4, Chem. Mater. 25 (2013) 503–508.

[21] M.J. Bojdys, J.O. Muller, M. Antonietti, A. Thomas, Ionothermal synthesis of crystalline, condensed, graphitic carbon nitride, Chem. Eur. J. 14 (2008) 8177–8182.

[22] F. Yang, V. Kuznietsov, M. Lublow, C. Merschjann, A. Steigert, J. Klaer, A. Thomas, T. Schedel-Niedrig, Solar hydrogen evolution using metal-free photocatalytic polymeric carbon nitride/CuInS2 composites as photocathodes, J. Mater. Chem. A 1 (2013) 6407–6415.

[23] X. Wang, K. Maeda, A. Thomas, K. Takanabe, G. Xin, J.M. Carlsson, A metal-free polymeric photocatalyst for hydrogen production from water under visible light, Nat. Mater. 8 (2009) 76–80.

[24] A.B. Yousaf, J.R. Monnier, J.W. Weidner, M.K. Hassan, S.J. Zaidi, P. Kasak, A precious-metal-free Fe-intercalated carbon nitride porous-network with enhanced activity for the oxygen reduction reaction and methanol-tolerant oxygen reduction reaction, Sustain. Energy Fuels 4 (10) (2020) 5050–5060.

[25] X. Xiao, J. Wei, Y. Yang, R. Xiong, C. Pan, J. Shi, Photoreactivity and mechanism of g-C_3N_4 and Ag Co-modified Bi2WO6 microsphere under visible light irradiation, ACS Sustain. Chem. Eng. 4 (2016) 3017–3023.

[26] S. Putla, M.H. Amin, B.M. Reddy, A. Nafady, K.A. Al-Farhan, S.K. Bhargava, MnOx nanoparticle-dispersed CeO2 nanocubes: a remarkable heteronanostructured system with unusual structural characteristics and superior catalytic performance, ACS Appl. Mater. Interfaces 7 (30) (2015) 16525–16535.

[27] H.J. Huang, Q. Chen, M.Y. He, X.Q. Sun, X. Wang, A ternary Pt/MnO2/graphene nanohybrid with an ultrahigh electrocatalytic activity toward methanol oxidation, J. Power Sources 239 (2013) 189–195.

[28] C. Xu, X. Wang, Fabrication of flexible metal-nanoparticle films using graphene oxide sheets as substrates, Small 5 (19) (2009) 2212–2217.

[29] Y. Omomo, T. Sasaki, Wang, M. Watanabe, Redoxable nanosheet crystallites of MnO_2 derived via delamination of a layered manganese oxide, J. Am. Chem. Soc. 125 (12) (2003) 3568–3575.

[30] J. Xu, S.W. Cao, T. Brenner, X.F. Yang, J.G. Yu, M. Antonietti, M. Shalom, Supramolecular chemistry in molten sulfur: preorganization effects leading to marked enhancement of carbon nitride photoelectrochemistry, Adv. Funct. Mater. 25 (2015) 6265–6271.

[31] S. Martha, A. Nashim, K.M. Parida, Facile synthesis of highly active g-C_3N_4 for efficient hydrogen production under visible light, J. Mater. Chem. A 1 (26) (2013) 7816.

[32] X.H. Li, M. Antonietti, Nitrogen-codoped holey graphene monoliths from molecules: carbocatalysts for selective oxidation, Angew. Chem. Int. Ed. 52 (2013) 4572–4576.

[33] Z.N. Liu, K.L. Xu, H. Sun, S.Y. Yin, One-step synthesis of single-layer MnO_2 nanosheets with multi-role sodium dodecyl sulfate for high-performance pseudocapacitors, Small 11 (18) (2015) 2182–2191.

[34] L.C. Chen, D.J. Huang, S.Y. Ren, T.Q. Dong, Y.W. Chi, G.N. Chen, Preparation of graphite-like carbon nitride nanoflake film with strong fluorescent and electrochemiluminescent activity, Nanoscale 5 (1) (2013) 225–230.

[35] J. Tian, Q. Liu, A.M. Asiri, A.O. Al-Youbi, X. Sun, Ultrathin graphitic carbon nitride nanosheet: a highly efficient fluorosensor for rapid, ultrasensitive detection of Cu^{2+}, Anal. Chem. 85 (2013) 5595–5599.

[36] J. Gao, Y. Zhou, Z.S. Li, S.C. Yan, N.Y. Wang, Z.G. Zou, High-yield synthesis of millimetre-long, semiconducting carbon nitride nanotubes with intense photoluminescence emission and reproducible photoconductivity, Nanoscale 4 (12) (2012) 3687.

[37] P.X. Qiu, H. Chen, C.M. Xu, N. Zhou, F. Jiang, X. Wang, Y.S. Fu, Fabrication of an exfoliated graphitic carbon nitride as a highly active visible light photocatalyst, J. Mater. Chem. A 3 (48) (2015) 24237–24244.

[38] P. Niu, L. Zhang, G. Liu, H.-M. Cheng, Graphene-Like carbon nitride nanosheets for improved photocatalytic activities, Adv. Funct. Mater. 22 (22) (2012) 4763–4770.

[39] A. Sumboja, C.Y. Foo, X. Wang, P.S. Lee, Large areal mass, flexible and free standing reduced graphene oxide/manganese dioxide paper for asymmetric supercapacitor device, Adv. Mater. 25 (20) (2013) 2809–2815.

[40] W. Xiao, D. Hu, C. Peng, G.Z. Chen, Interfacial synthesis: amphiphilic monomer assisted ultrarefining of mesoporous manganese oxide nanoparticles and the electrochemical implications, ACS Appl. Mater. Interfaces 3 (2011) 3120–3129.

[41] G.A. Filonenko, R.V. Putten, E.J.M. Hensen, E.A. Pidko, Catalytic (de) hydrogenation promoted by non-precious metals – Co, Fe and Mn: recent advances in an emerging field, Chem. Soc. Rev. 47 (2018) 1459–1483.

[42] P. Xia, B. Zhu, B. Cheng, J. Yu, J. Xu, 2D/2D g-C_3N_4/MnO_2 nanocomposite as a direct Zscheme photocatalyst for enhanced photocatalytic activity, ACS Sustain. Chem. Eng. 6 (1) (2018) 965–973.

[43] T. Aditya, J. Jana, A. Pal, T. Pal, One-pot fabrication of perforated graphitic carbon nitride nanosheets decorated with copper oxide by controlled ammonia and sulfur trioxide release for enhanced catalytic activity, ACS Omega 3 (2018) 9318–9332.

[44] P. Xia, S. Cao, B. Zhu, M. Liu, M. Shi, J. Yu, Y. Zhang, Designing 0D/2D S-scheme heterojunction over polymeric carbon nitride for visible-light photocatalytic inactivation of bacteria, Angew. Chem. Int. Ed. 59 (13) (2020) 5218–5225.

[45] C. Wang, F. Yang, W. Yang, L. Ren, Y. Zhang, X. Jia, L. Zhang, Y. Li, PdO nanoparticles enhancing the catalytic activity of Pd/carbon nanotubes for 4-nitrophenol reduction, RSC Adv. 5 (35) (2015) 27526–27532.

[46] S. Asaoka, H. Okamura, Y. Akita, K. Nakano, K. Nakamoto, T. Hino, T. Saito, S. Hayakawa, M. Katayama, Y. Inada, Regeneration of manganese oxide as adsorption sites for hydrogen sulfide on granulated coal ash, Chem. Eng. J. 254 (2014) 531–537.

[47] F MORALES, E DESMIT, F DEGROOT, T VISSER, B WECKHUYSEN, Effects of manganese oxide promoter on the CO and H_2 adsorption properties of titania-supported cobalt fischer-tropsch catalysts, Journal of Catalysis 246 (1) (2007) 91–99.

[48] B. Mattson, W. Foster, J. Greimann, T. Hoette, N. Le, A. Mirich, S. Wankum, A. Cabri, C. Reichenbacher, E. Schwanke, Heterogeneous catalysis: the horiuti–polanyi mechanism and alkene hydrogenation, J. Chem. Educ. 90 (5) (2013) 613–619.

[49] L. Xin, A.L. Jin, Y.S. Jia, T.L. Xia, C.X. Deng, M.H. Zhu, C.F. Chen, X.S. Chen, Synergy of adsorption and visible-light photocatalytic degradation of methylene blue by a bifunctional Z-scheme heterojunction of WO_3/g-C_3N_4, Appl. Surf. Sci. 405 (2017) 359–371.

[50] L.M. Sun, Y. Qi, C.-J. Jia, Z. Jin, W.L. Fan, Enhanced visible-light photocatalytic activity of g-C_3N_4/Zn_2GeO_4 heterojunctions with effective interfaces based on band match, Nanoscale 6 (5) (2014) 2649.

[51] Y. He, D.B. Jiang, J. Chen, D.Y. Jiang, Y.X. Zhang, Synthesis of MnO_2 nanosheets on montmorillonite for oxidative degradation and adsorption of methylene blue, J. Colloid and Interf. Sci. 510 (2018) 207–220.

[52] G. Cheng, L. Yu, T. Lin, R. Yang, M. Sun, B. Lan, L. Yang, F. Deng, A facile one-pot hydrothermal synthesis of β-MnO_2 nano pincers and their catalytic degradation of methylene blue, J. Solid State Chem. 217 (2014) 57–63.

[53] F.J. Wu, X. Li, W. Liu, S.T. Zhang, Highly enhanced photocatalytic degradation of methylene blue over the indirect all-solid-state Z-scheme g-C_3N_4/RGO/TiO_2 nanoheterojunctions, Appl. Surf. Sci. 405 (2017) 60–70.

[54] M.S. El-Deab, T. Ohsaka, Manganese oxide nanoparticles electrodeposited on platinum are superior to platinum for oxygen reduction, Angew. Chem., Int. Ed. 45 (2006) 5963.

[55] Y. Meng, W. Song, H. Huang, Z. Ren, S.Y. Chen, S.L. Suib, Structure-property relationship of bifunctional MnO_2 nanostructures: highly efficient, ultra-stable electrochemical water oxidation and oxygen reduction reaction catalysts identified in alkaline media, J. Am. Chem. Soc. 136 (2014) 11452–11464.

[56] F. Cheng, T. Zhang, Y. Zhang, J. Du, X. Han, J. Chen, Enhancing electrocatalytic oxygen reduction on MnO_2 with vacancies, Angew. Chem., Int. Ed. 52 (2013) 2474–2477.